JGR Atmospheres

RESEARCH ARTICLE
10.1029/2023JD039936

Comparison of Short-Term Cloud Feedbacks at Top of the Atmosphere and the Surface in Observations and AMIP6 Models

Xiaocong Wang[1], Hao Miao[2], Juan Feng[3], and Yimin Liu[1]

[1]State Key Laboratory of Numerical Modeling for Atmospheric Sciences and Geophysical Fluid Dynamics, Institute of Atmospheric Physics, Chinese Academy of Sciences, Beijing, China, [2]Key Laboratory of Transportation Meteorology of China Meteorological Administration, Nanjing Joint Institute for Atmospheric Sciences, Nanjing, China, [3]Center for Monsoon System Research, Institute of Atmospheric Physics, Chinese Academy of Sciences, Beijing, China

Key Points:

- The intermodel spread of the net short-term cloud feedback is larger at the surface and within the atmosphere than at the top of atmosphere
- An inverse relationship between cloud feedbacks in the El Niño–Southern Oscillation (ENSO) and non-ENSO regions is found in both observations and AMIP6 models
- Compared to observations, models tend to overestimate longwave cloud feedback in ENSO regions due to the overestimation of high-topped cloud

Supporting Information:

Supporting Information may be found in the online version of this article.

Correspondence to:

X. Wang,
wangxc@lasg.iap.ac.cn

Citation:

Wang, X., Miao, H., Feng, J., & Liu, Y. (2024). Comparison of short-term cloud feedbacks at top of the atmosphere and the surface in observations and AMIP6 models. *Journal of Geophysical Research: Atmospheres*, *129*, e2023JD039936. https://doi.org/10.1029/2023JD039936

Received 6 SEP 2023
Accepted 10 JAN 2024

Abstract

We compared short-term cloud feedback, defined at the top of the atmosphere (TOA), the atmospheric column (ATM), and the surface (SFC), between observations and models participating in Atmospheric Model Intercomparison Project Phase 6 (AMIP6) for the period 2000–2014. The globally averaged net cloud feedbacks observed at TOA, ATM, and SFC are -0.06 ± 0.63, -0.17 ± 0.70, and 0.11 ± 0.81 W m^{-2} K^{-1}, respectively. While most models produced TOA cloud feedbacks that agreed with the observations within uncertainty ranges, the intermodel spread at SFC and within ATM was relatively larger. This demonstrates that models are diverse in how their TOA feedback is distributed between ATM and SFC. Because short-term cloud feedback is mainly driven by El Niño–Southern Oscillation (ENSO), the global-mean cloud feedback was further decomposed into components from the ENSO and non-ENSO regions. Results show that cloud feedback in these two regions tends to be inversely related. Compared to observations, almost all models overestimated the longwave cloud feedback in the ENSO region due to the overestimation of cloud amount changes for high-topped clouds. For these models, it is the offset between deviations in ENSO and non-ENSO regions that leads to the overall agreement of global mean with observations. Sensitivity tests show that the main conclusions still hold when alternative kernels are used in estimating cloud feedback.

Plain Language Summary

The large spread in cloud feedback among climate models contributes to the largest uncertainty in climate sensitivity. There is an urgent need to utilize observational data to validate cloud feedback in climate models. By using a combination of reanalysis data and satellite measurements for the period 2000–2014, results show the observed cloud feedback at TOA, ATM, and SFC is -0.06 ± 0.63, -0.17 ± 0.70, and 0.11 ± 0.81 W m^{-2} K^{-1}, respectively. Most models produced TOA cloud feedback that was consistent with observations within the uncertainty range, yet there was larger difference at the surface and within the atmosphere, causing some models to produce values outside the uncertainty range. Further study shows that even well-modeled TOA feedback is due to bias offsetting. The models tend to overestimate longwave cloud feedback in the El Niño–Southern Oscillation (ENSO) region due to an overestimation of high-topped cloud changes, which is partially offset by an underestimation in the non-ENSO region, resulting in a global mean that is close to the observed value. Decomposing cloud response and cloud feedback in this way highlights the deficiency in ENSO-related cloud modeling that would otherwise be hidden by the global average.

1. Introduction

It is well recognized that much of the global warming currently being experienced and expected to occur comes from climate feedback processes that amplify or damp the initial radiative perturbation (Sherwood et al., 2020). Positive feedbacks such as albedo and water vapor, act to enhance the response to the forcing, whereas temperature feedback acts to counteract the forcing and is therefore considered as a negative feedback. While there is relatively good agreement on non-cloud feedbacks between different models (Colman, 2003; Soden et al., 2008; Wang et al., 2023; Zhang et al., 2020), there is no clear consensus on cloud feedback, which roughly ranges from −0.3 to 1.2 W m^{-2} K^{-1} in Coupled Model Intercomparison Project Phase 6 models (Zelinka et al., 2020). In fact, cloud feedback has long been recognized as the largest source of uncertainty in climate sensitivity (Stephens, 2005; Zhang et al., 1994), defined as the global temperature rise under the forcing of doubled carbon dioxide (CO_2)

concentration. To this end, there is an urgent need to use observational data to validate cloud feedback in climate models. Unfortunately, the lack of long-term observations, especially for radiative flux measurements from satellites, makes it difficult to estimate long-term cloud feedback from observations. However, current observations are sufficient to estimate short-term cloud feedbacks driven primarily by El Niño–Southern Oscillation (ENSO) (Dessler, 2010, 2013; Wang et al., 2020; Zhao et al., 2022; Zhou et al., 2015). Although cloud feedback determined for short-term climate variations is distinguished from those determined for long-term climate changes because of differences in surface warming pattern on the two timescales (Colman & Power, 2010; Zhou et al., 2015; Zhu et al., 2007), validation of the former is an important step in increasing our confidence in the latter.

Cloud feedback is typically defined at the top of the atmosphere (TOA), while climate sensitivity refers to temperature changes at the surface. The underlying rationale is that on the timescale of climate change, the heat capacity of the atmosphere is so small that any TOA energy imbalance must be manifested at the surface. However, in some cases, the TOA feedback needs to be decomposed into components from the atmospheric column (ATM) and the surface (SFC). For example, precipitation changes are more relevant to the atmospheric energy constraint. Under global warming, the atmosphere is expected to lose more radiative energy primarily due to increased longwave emission as a result of warmer temperature. This then requires a compensatory increase in atmospheric latent heating associated with greater precipitation (Allen & Ingram, 2002; Mitchell et al., 1987). There has been increasing progress to quantify and understand cloud feedback that influences the rate of change of precipitation in a warming climate (Previdi, 2010; Stephens & Ellis, 2008). On the other hand, surface temperature changes are more relevant to adjustments in the surface energy balance (Lu & Cai, 2009). In short, while the TOA feedback regulates climate sensitivity, the ATM feedback regulates the response of the hydrological cycle to climate change (Andrews et al., 2009; Previdi, 2010). Therefore, exploring how clouds regulate energy through the atmosphere-surface column is critical to understanding climate and hydrological sensitivity.

While cloud feedback defined at TOA has been extensively studied (Ceppi et al., 2017; Liu et al., 2022; Sherwood et al., 2020; Wang et al., 2022; Zelinka et al., 2022; Zhang et al., 2018, 2020), relatively few studies have been conducted on cloud feedback defined at SFC and within ATM (Lambert et al., 2015; Previdi, 2010; Previdi & Liepert, 2012). In this study, we first estimated the observed cloud feedback from TOA, ATM, and SFC using a combination of reanalysis data and satellite measurements for the period 2000–2014. The observed cloud feedbacks were then used to validate cloud feedbacks estimated from models participating in AMIP6. With the aid of cloud radiative kernel technique, differences between models and observations can be attributed to the simulation of specific cloud types stratified by cloud optical depth and cloud top height, which helps to understand the causes of cloud feedback bias in models. As short-term cloud feedback is tightly related with ENSO, further attention is paid to contrasting cloud feedbacks in ENSO (100°E−100°W, 20°S–20°N) and non-ENSO (remaining) regions. Under this division, some extratropical regions remotely linked to ENSO are categorized as non-ENSO regions, and thus ENSO teleconnections in the non-ENSO regions are not being accounted for. Decomposing cloud feedback in this way highlights the deficiency in cloud modeling associated with ENSO that would be otherwise hidden by the global average.

The remainder of this paper is organized as follows. Section 2 describes the data and methodology. Section 3 diagnoses and compares cloud feedbacks defined at TOA, ATM, and SFC in observations and AMIP6 models. The discrepancy between models and observations are attributed to differences in the simulation of specific cloud types stratified by cloud optical depth and cloud top height. Also explored in this section is the sensitivity of the estimated cloud feedback to the different kernels used. Finally, the last section concludes with a summary.

2. Data and Methodology

2.1. Methodology for Cloud Feedback Estimation

Two different methods are used to estimate cloud feedbacks: (a) the method of adjusting the change in cloud radiative effect (ΔCRE) that is defined by the difference between the all-sky radiation flux and the clear-sky flux, taking into account the masking effects of clouds (Shell et al., 2008; Soden et al., 2008); and (b) the cloud radiative kernel technique (Zelinka et al., 2012).

In the first method, ΔR_{cloud} (changes in radiative flux due to clouds) is calculated by subtracting the cloud masking effects of changing temperature (ΔT), water vapor (Δq) and surface albedo (Δa) from the change in cloud radiative effect (ΔCRE):

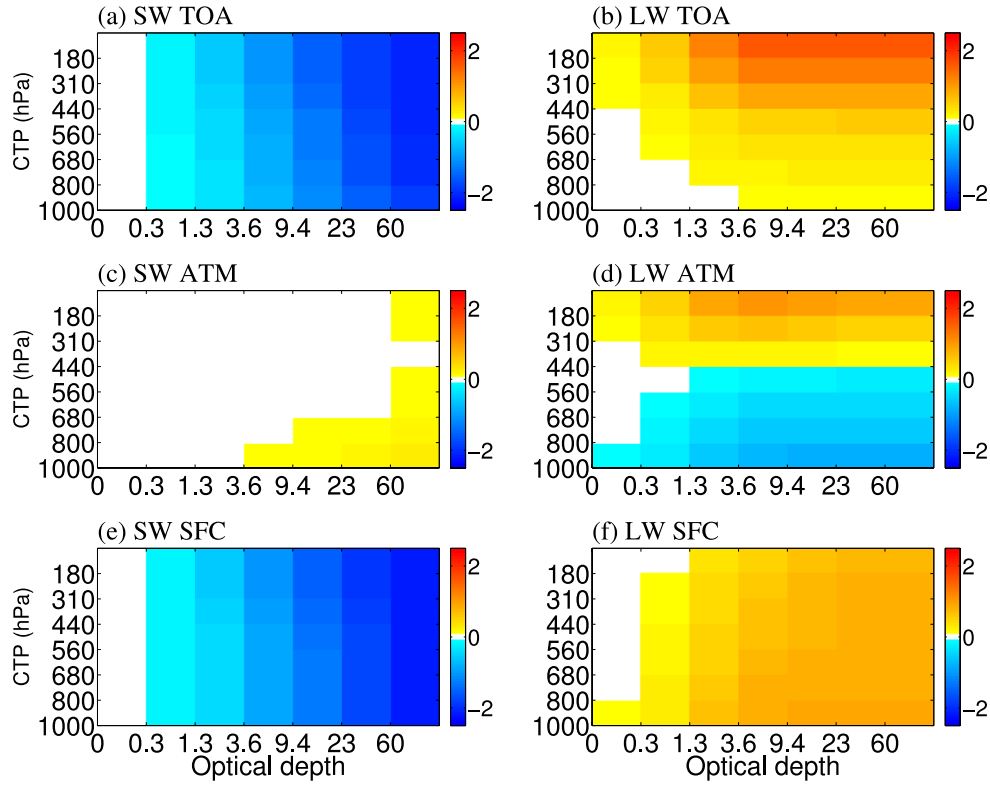

Figure 1. Global and annual mean SW (a, c, e) and LW (b, d, f) cloud radiative kernels at top of the atmosphere (a, b), atmospheric column (c, d), and SFC (e, f) from Zhou's kernel. (Unit: W $m^{-2}\%^{-1}$).

$$\Delta R_{\text{cloud}} = \Delta\text{CRE} + \left(K_T^0 - K_T\right)\Delta T + \left(K_q^0 - K_q\right)\Delta q + \left(K_a^0 - K_a\right)\Delta a, \tag{1}$$

where K_T, K_q and K_a are radiative kernels for temperature, water vapor and surface albedo, respectively, with superscript "0" standing for clear sky. Equation 1 applies for both TOA and SFC. In this study, the observation-based radiative kernel from CloudSat/CALIPSO (Kramer et al., 2019) was used to break down the feedback into individual components. Following Soden et al. (2008), the tropospherically averaged results integrated from the surface to the tropopause, defined as 100 hPa at the equator and decreasing linearly with latitude to 300 hPa at the poles, are used to study the sensitivity of TOA flux to tropospheric perturbations,

In the second method, ΔR_{cloud} is estimated by multiplying the change in cloud fraction (ΔC) for each International Satellite Cloud Climatology Project (ISCCP) cloud type by the corresponding cloud radiative kernel:

$$\Delta R_{\text{cloud}}\left(\text{lon}, \text{lat}, P_{\text{top}}, \tau\right) = \frac{\partial R}{\partial C}\left(P_{\text{top}}, \tau\right) \times \Delta C\left(\text{lon}, \text{lat}, P_{\text{top}}, \tau\right), \tag{2}$$

where ΔR_{cloud} (lon, lat, P_{top}, τ) is the contribution to the radiative flux anomaly at a particular location and for clouds with a particular cloud top pressure P_{top} and cloud optical depth τ. The term $\frac{\partial R}{\partial C}\left(P_{\text{top}}, \tau\right)$ represents cloud radiative kernel, which is defined at each latitude and is given for each month of the seasonal cycle. We use the TOA and SFC cloud radiative kernels developed by Zhou et al. (2022), which were built using a radiative transfer model initialized with atmospheric and surface conditions from ERA-Interim reanalysis data. Given that cloud property histograms are usually functions of P_{top} and τ, the SFC kernel on P_{bot}-τ histograms was converted to P_{top}-τ fields based on the statistical relationship between P_{top}, P_{bot} and τ, where P_{bot} stands for cloud bottom pressure. Zhou et al. (2022) achieved this by jointly utilizing CloudSat data providing P_{bot} and Moderate Resolution Imaging Spectroradiometer (MODIS) products providing P_{top} and τ to construct P_{bot} -P_{top} -τ joint histograms.

Figure 1 shows the global and annual mean shortwave (SW) and longwave (LW) cloud radiative kernels at TOA, ATM, and SFC, where each bin represents the contribution to the radiative flux anomaly for a particular cloud type. The SW cloud radiative kernel is negative for all cloud types at TOA and SFC, indicating that increases in

Table 1
List of AMIP6 Models in This Study

Model	Host institute	Resolution
BCC-CSM2-MR	Beijing Climate Center, China Meteorological Administration, China	$1.125^\circ \times 1.125^\circ$
CESM2	National Center for Atmospheric Research, USA	$1.25^\circ \times 0.9375^\circ$
CanESM5	Canadian Centre for Climate Modeling and Analysis, Canada	$2.8125^\circ \times 2.8125^\circ$
E3SM-1-0	The United States Department of Energy (DOE), USA	$1^\circ \times 1^\circ$
GFDL-CM4	NOAA Geophysical Fluid Dynamics Laboratory, USA	$1.25^\circ \times 1^\circ$
GISS-E2-1-G	NASA Goddard Institute for Space Studies, USA	$2.5^\circ \times 2^\circ$
HadGEM3-GC31-LL	Met Office Hadley Centre, UK	$1.875^\circ \times 1.25^\circ$
MIROC6	University of Tokyo, Japan	$1.4^\circ \times 1.4^\circ$
MRI-ESM2-0	Meteorological Research Institute, Japan	$1.125^\circ \times 1.125^\circ$

cloud fraction result in increases in SW reflection to space and vice versa. Within ATM, small positive values occur at thick optical depth bins due to weak absorption of SW by clouds. Regarding the LW component, the kernel is positive for all cloud types at TOA and increases with decreasing P_{top}. In terms of the SFC response, the LW cloud radiative kernel is also positive but decreases with decreasing P_{top}. With regard to the ATM response, the kernel is positive for mid- and high-topped clouds, and negative for low-topped clouds. This is due to the fact that low-topped clouds are inefficient in preventing longwave radiation from TOA, but more efficient at enhancing downward longwave emission to SFC.

For both the adjusting method and the cloud radiative kernel technique, ΔR_{cloud} anomalies at TOA and SFC were first calculated by subtracting the climate mean from each month's value; then cloud feedback at TOA and SFC were obtained by regressing the corresponding anomalies onto the global mean surface temperature anomaly (ΔT_s), following the method of Gregory et al. (2004). Cloud feedback within ATM is obtained from the difference between cloud feedback at TOA and SFC.

2.2. Data Description

The observed temperature, moisture, and surface albedo anomalies in Equation 1 are calculated using monthly averaged ERA-Interim reanalysis (Dee et al., 2011), while ΔCRE at TOA and SFC is derived from the Cloud and the Earth's Radiant Energy System (CERES). The cloud fraction anomalies in Equation 2 are calculated using cloud observations from MODIS on board the Terra satellite (Platnick et al., 2015), along with the ISCCP product (Young et al., 2018) used as a comparator.

The models investigated in this study include those participating in AMIP6 (Eyring et al., 2016), and were chosen based on the availability of cloud simulator output. Information about these models is presented in Table 1. The time period for all data sets used is from March 2000 to December 2014, allowing for maximum overlap between observational and model products. We use the same time period in observations and model simulations because short-term cloud feedback may be different when different time periods is used due to the dependence on the surface warming pattern (Chao et al., 2022; Loeb et al., 2020; Wang et al., 2023; Zhou et al., 2016).

3. Results and Analysis

Figure 2a shows the time series of monthly and global average anomalies of ΔT_s (pink), as well as the ENSO index (blue), defined as the sea surface temperature (SST) anomalies averaged over the central and eastern Pacific (5°S-5°N, 170°W-120°W). The trend appears to be flat because of the hiatus during 1998–2013, with a smaller warming rate compared to the warming in the latter half of the twentieth century (Yan et al., 2016). The close association between ΔT_s and the ENSO index verifies that the climate variation over this period is mainly associated with ENSO, where the correlation between ΔT_s and the ENSO index is 0.49 (p-value <0.01). Figure 2b shows the time series of TOA longwave ΔR_{cloud} anomalies calculated using Equation 1 (black) and Equation 2 (pink). Also overlaid is the blue curve calculated using ISCCP observations in Equation 2. The adjusting method and the cloud radiative kernel technique produce similar magnitudes of ΔR_{cloud} when using MODIS observations, yet considerable differences are found when using ISCCP observations, with a root-mean-square error of 0.58 for

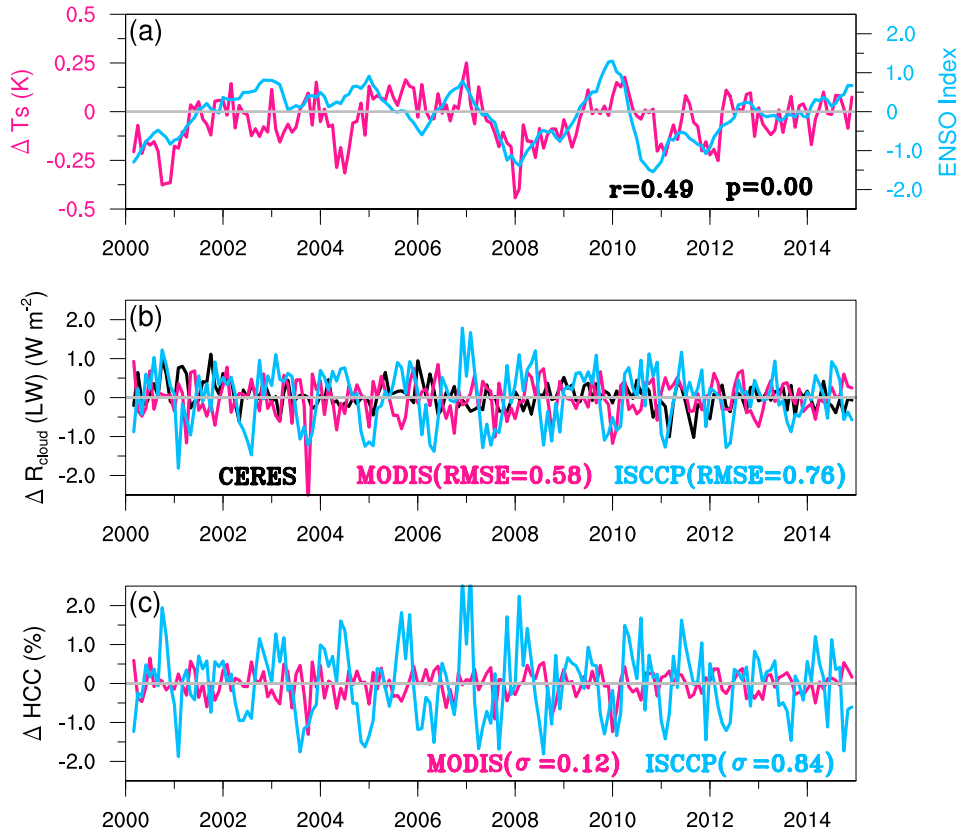

Figure 2. (a) Global average ΔT_s (pink) and El Niño–Southern Oscillation index (blue) calculated from ERA-Interim reanalysis. (b) Global averaged longwave ΔR_{cloud} calculated from Cloud and the Earth's Radiant Energy System measurements using the adjusting method (black), and from Moderate Resolution Imaging Spectroradiometer (MODIS) (pink) and International Satellite Cloud Climatology Project (ISCCP) (blue) observations using the cloud kernel technique. (c) Global average anomaly of high-topped clouds from MODIS (pink) and ISCCP (blue) observations.

the former and 0.76 for the latter. The relatively larger oscillation of ΔR_{cloud} in ISCCP is consistent with larger oscillation of high-topped clouds ($p < 440$ hPa) shown in Figure 2c, with the standard deviation reaching as high as 0.84 compared to 0.12 in MODIS. As claimed in Marchand (2013), there is considerable concern about the stability of ISCCP-derived cloud fractions due to changes in constellation, and caution must be exercised when using ISCCP component cloud fractions for trend analysis. It is for this reason that we decided not to use ISCCP observations in the following sections, even though the ISCCP-retrieved cloud top is more consistent with the cloud radiative kernel (Zhou et al., 2013).

3.1. Observed Short-Term Cloud Feedback at TOA, ATM, and SFC

Figure 3 shows the observed spatial distribution of cloud feedback at TOA (top), ATM (middle), and SFC (bottom), which are calculated from CERES observations using Equation 1. We distinguish between SW (left) and LW (middle) components and also display their sum (right), which we call "NET." The sign convention is that positive values indicate an increase in radiative heating, that is, positive for downward fluxes at TOA and SFC. For both SW and LW cloud feedbacks at TOA (Figures 3a and 3b), there is a characteristic dipole pattern in the tropical Pacific, with negative SW feedback in the central Pacific and positive SW feedback in the western Pacific. For the LW component, there is positive feedback in the central Pacific and negative feedback in the western Pacific, which is a consequence of typical reorganization associated with ENSO. Raghuraman et al. (2019) also found a similar pattern for almost the same time period for the greenhouse effect. The globally averaged SW feedback of 0.06 W m^{-2} K^{-1} and LW feedback of −0.04 W m^{-2} K^{-1} largely cancel each other out, a consequence of the fact that clouds both trap LW radiation and reflect SW radiation back to space, resulting in much smaller NET cloud feedback of 0.02 W m^{-2} K^{-1} (Figure 3c). Because SW is in general weakly absorbed by clouds, the SW cloud feedback at each grid point within the ATM is small (Figure 3d), although the global mean reaches as

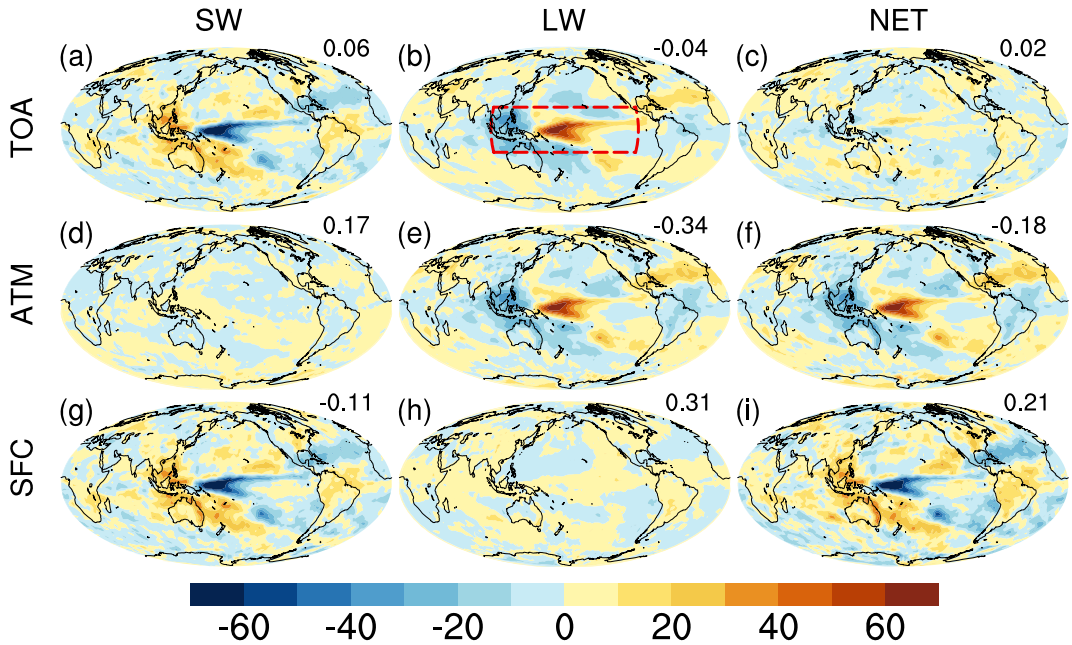

Figure 3. Spatial distribution of the short-term cloud feedback at top of the atmosphere (a–c), atmospheric column (d–f), and SFC (g–i) calculated from Cloud and the Earth's Radiant Energy System measurements using the adjusting method. The left, middle, and right columns are the SW, LW, and NET components. In panel (b), the red rectangle stands for the El Niño–Southern Oscillation region (100°E−100°W, 20°S–20°N). The global mean value is shown in the top right of each figure. Unit: W m^{-2} K^{-1}.

large as 0.17 W m^{-2} K^{-1}. The patten of LW cloud feedback within the ATM bears close resemblance to that at TOA, with a large negative global mean of −0.34 W m^{-2} K^{-1} due to downward LW emission to SFC.

While SW and LW feedbacks at TOA are strongly affected by ENSO, the LW at SFC (Figure 3h) is not, where the ENSO signal is only marginally observed. To understand the reason, we show in Figure S1 in Supporting Information S1 the changes in cloud fraction per degree increase for different cloud types stratified by cloud top height. Essentially, the LW cloud feedback at SFC is driven by the location of cloud bottom and is not sensitive to the position of cloud top, so clouds with different cloud top height all contribute to the surface heating. As noticed, low-topped clouds ($p > 680$ hPa, Figure S1c in Supporting Information S1) are less influenced by ENSO and tend to be inversely related to high-topped clouds ($p < 440$ hPa) in the same geographical location, in agreement with the findings of Zhu et al. (2007). Changes in emissions from these two types of clouds may cancel each other out, resulting in a relatively small heating at SFC.

The difference between cloud feedback calculated from MODIS observations using Equation 2 against those calculated from CERES observations using Equation 1 is shown in Figure S2 in Supporting Information S1. In general, the MODIS results agree well with the CERES results at TOA, with most of the grid point differences within the range of 5 W m^{-2} K^{-1}. Within ATM and at SFC, the differences in LW cloud feedback are relatively larger than those seen at TOA. Possible reasons are as follows. One is the limitation of passive instrument such as MODIS in detecting low-topped clouds, which are more likely to be obscured by high-topped clouds. In addition, the statistical relationship used to convert P_{bot}-τ histograms to P_{top}-τ fields in the construction of the surface kernel is also responsible for the discrepancy (Zhou et al., 2022). However, this has much less of an effect on the SW component.

3.2. Short-Term Cloud Feedback Estimated From AMIP6 Models

In this subsection, the observed cloud feedbacks were used to evaluate cloud feedbacks estimated from models participating in AMIP6. Figure 4 shows the difference in cloud feedback between multimodel mean and the observations at TOA (top), ATM (middle), and SFC (bottom) using the adjusting method. The difference map between cloud feedbacks calculated using the cloud radiative kernel technique against those calculated using

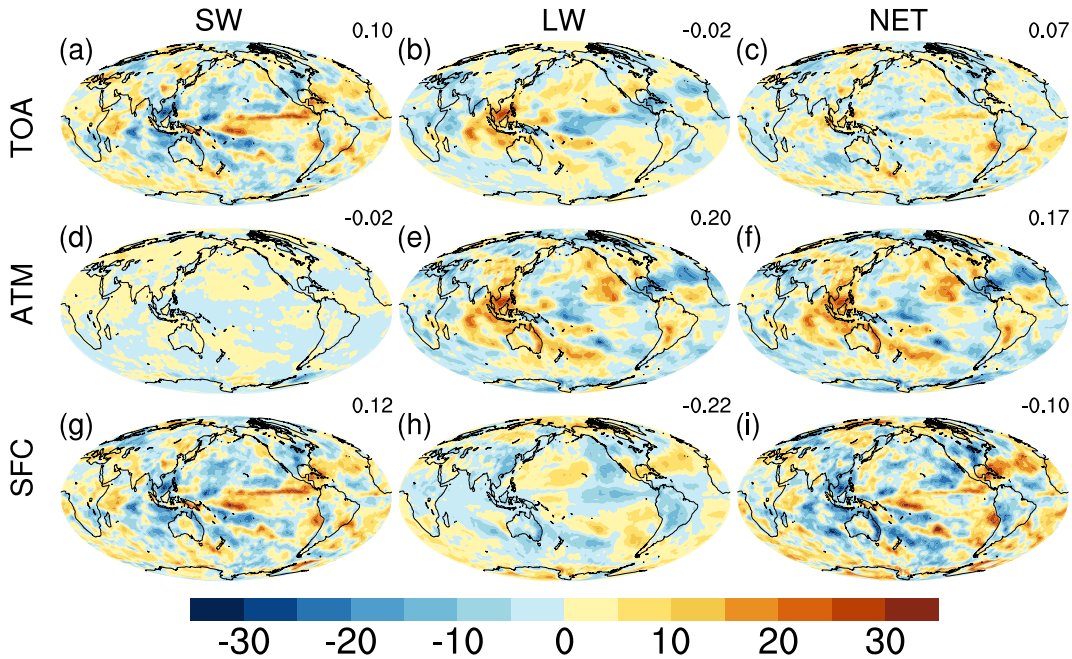

Figure 4. Differences in cloud feedback between multimodel mean and the observation at top of the atmosphere (a–c), atmospheric column (d–f), and SFC (g–i) under the adjusting method. The left, middle, and right columns are the SW, LW, and NET components. The global mean value is shown in the top right of each figure. Unit: W m^{-2} K^{-1}.

the adjusting method is shown in Figure S3 in Supporting Information S1. For LW cloud feedback at TOA (Figure 4b), there is a positive bias of up to 20 W m^{-2} K^{-1} over the eastern Indian Ocean and Maritime continent regions, and a negative bias of similar magnitude along the central to the eastern Pacific. Since LW cloud feedback at TOA is mainly influenced by high-topped clouds, Figure 5 presents the difference in high-topped cloud response between models and the observations. In the Maritime continent regions, models commonly overestimated the simulation of cloud amount for high-topped clouds in response to surface temperature changes on interannual timescales, with the multimodel mean deviation of up to 10% K^{-1}. While the overestimation of LW cloud feedback coincides with the overestimation of high-topped clouds in the Maritime continent regions, the correspondence is less well established in the eastern Pacific. This is due to the prevalence of low-topped clouds in the eastern Pacific, which largely influence the relationship between LW cloud feedback and high-topped clouds. Moreover, models exhibit large diversity in the response of high-topped clouds in the eastern Pacific. While BCC-CSM2-MR and GISS-E2-1-G overestimated the simulation of cloud fraction for high-topped clouds, the MRI-ESM2-0 model underestimated them instead. This demonstrates that some important aspects of ENSO variability are still poorly simulated in current models.

The cloud feedback differences at TOA can be ascribed to differences at SFC and ATM. For SW, which is weakly absorbed by clouds in general, the difference pattern is tracked by that at SFC (Figure 4g), while for LW, which is strongly absorbed and emitted by clouds, it is tracked by that within ATM (Figure 4e). Unlike the case of TOA, where the bias of net cloud feedback is small owing to large cancellation between SW and LW components, there are considerable biases of up to 25 W m^{-2} K^{-1} in the net cloud feedback within ATM and at SFC in the Maritime continent regions. This demonstrates that the estimation of net cloud feedback at SFC and ATM demands on higher accuracy of the SW and LW components, which should be scrutinized in detail (Miao et al., 2021).

To explore these differences more concisely, Figure 6 compares the SW, LW, and NET cloud feedback for the observation and multimodel mean as a function of latitude, with shading denoting the width of twice the standard deviation of the results of all participating models. Only cloud feedback estimated using the cloud kernel technique is shown. The observed SW feedback at TOA shows a negative peak in the deep tropics (10°S–10°N) and two positive peaks within 10°–25° in both hemispheres, which then tend to be flattened toward high latitudes. While the peak over the equator was well captured by the multimodel mean, the peak centered at 15°S was underestimated, with the multimodel mean bias reaching as large as 4 W m^{-2} K^{-1}, and this is where the inter-

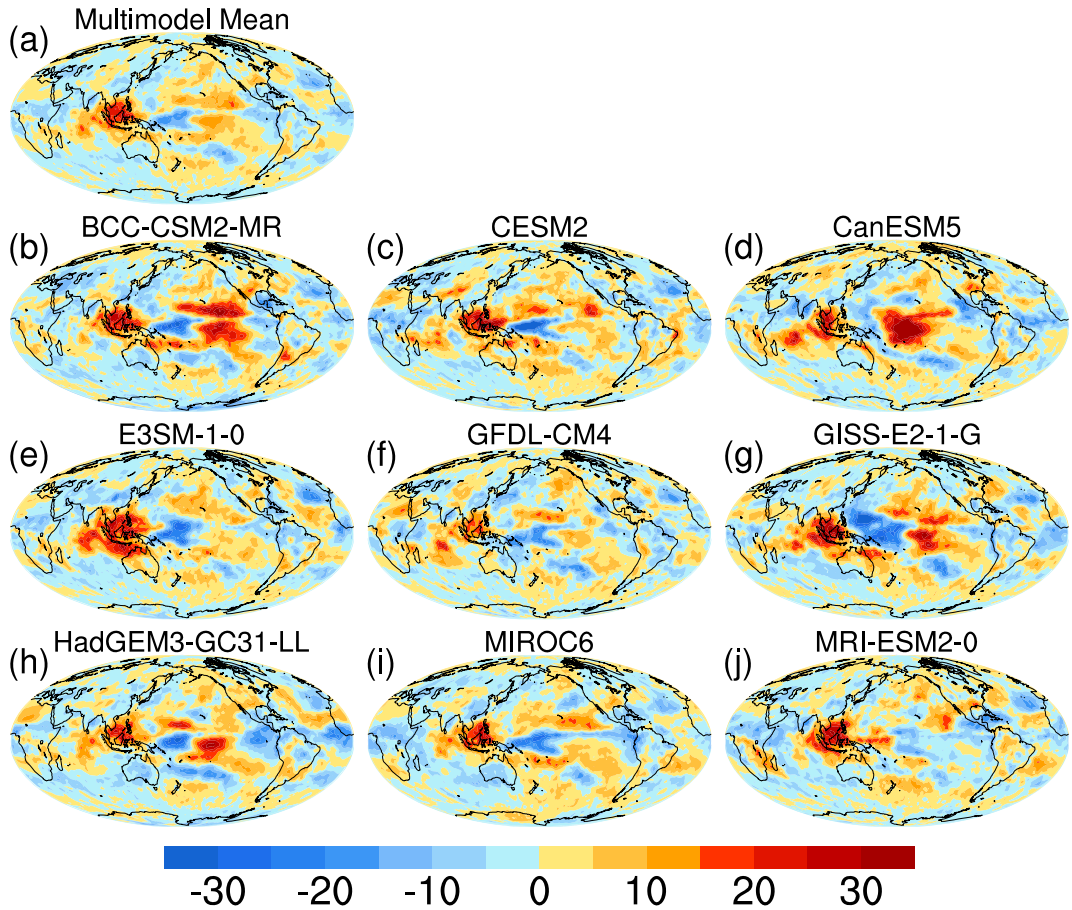

Figure 5. Differences of high-topped cloud changes between AMIP6 models and the Moderate Resolution Imaging Spectroradiometer observation. Unit: % K^{-1}.

model spread is greatest. The finding is consistent with previous studies pointing out clouds in the subtropics contribute to the largest uncertainty in cloud feedback (Bony & Dufresne, 2005; Cesana et al., 2017). The TOA LW feedback is almost a mirror image of the TOA SW feedback, which largely offsets the bias of SW feedback, resulting in smaller biases in the NET feedback (Figure 6c). Since solar energy is only weakly absorbed by clouds, the SW feedback within ATM is close to zero (Figure 6d). The patten of ATM NET feedback tracks that of LW feedback, where the multimodel mean underestimated the magnitude in the subtropics compared to observations. At SFC, the multimodel mean shows a slight underestimation of LW feedback in the tropics, which partially offsets the underestimation of SW feedback, leading to a relatively small bias in NET feedback (Figure 6i).

3.3. Cloud Feedback in ENSO and Non-ENSO Regions

Figure 7 summarizes the global average cloud feedback at TOA, ATM, and SFC for observations and models. The error bar in solid circles represents the 95% confidence range in observations, estimated as twice the standard error of the slope of the fit, while the error bar in open circles represents the 95% confidence range for multimodel mean. The global average cloud feedbacks are also summarized in Tables 2 and 3. The TOA net cloud feedback is 0.02 ± 0.57 W m^{-2} K^{-1} for the adjusting method and -0.14 ± 0.69 W m^{-2} K^{-1} for the cloud radiative kernel technique, which stand in contrast to the large net cloud feedback of 0.4–0.7 W m^{-2} K^{-1} in previous studies (Chao et al., 2022; Dessler, 2010, 2013), yet is comparable to the results of -0.16 ± 0.83 W m^{-2} K^{-1} in Zhou et al. (2013) and 0.20 ± 0.34 W m^{-2} K^{-1} in Raghuraman et al. (2023). Both methods show that the observed ATM net cloud feedback is about -0.17 W m^{-2} K^{-1}, suggesting cloud changes act to increase the radiative cooling of the atmosphere during the period 2000–2014.

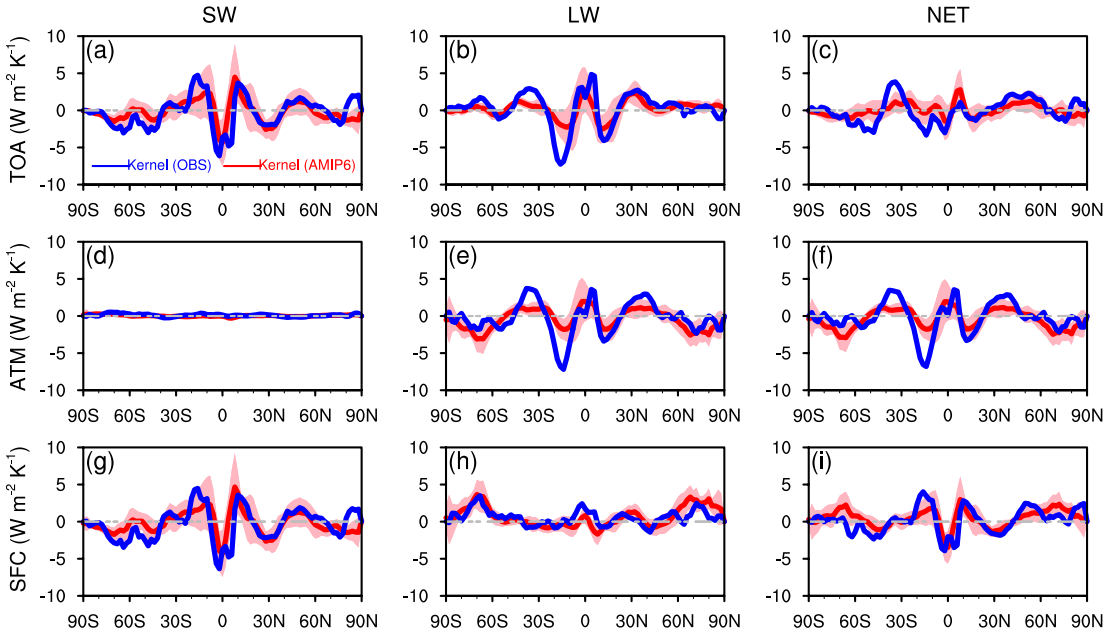

Figure 6. Zonally averaged short-term cloud feedbacks for the observation and multimodel mean at top of the atmosphere (a–c), atmospheric column (d–f), and SFC (g–i) using the cloud radiative kernel technique. The left, middle, and right columns are for SW, LW and NET cloud feedback, respectively. The shading indicates the width of twice the standard deviation of the results of all AMIP6 models.

For either observation or models, cloud feedbacks estimated by the two techniques are generally consistent, with the differences mostly falling within the range of 0.2 W m^{-2} K^{-1}. The net cloud feedback in models ranges roughly from −0.4 to 0.5 W m^{-2} K^{-1} at TOA, from −0.6 to 0.6 W m^{-2} K^{-1} within ATM, and from −0.6 to 1.0 W m^{-2} K^{-1} at SFC, which overall coincides with the uncertainty range of observations. While most models produced global average feedback that agreed, within uncertainty ranges, with the observations, a few models produced values that lay outside the uncertainty range. For instance, at TOA and SFC, MIROC6 overestimates the SW cloud feedback and underestimates the LW cloud feedback. Although models may have similar feedback at TOA, they may differ substantially in how the TOA feedback is distributed between SFC and ATM. For example, CanESM5 and GISS-E2-1-G have similar LW feedback at TOA, close to 0.8 W m^{-2} K^{-1} estimated using the cloud kernel technique, yet it is almost entirely due to the ATM component in the former (more than 83%), while the SFC component account for more than 45% in the latter.

Because short-term cloud feedback is tightly associated with ENSO, the global average feedback was further decomposed into two components—one from the ENSO region (red box in Figure 3b) and the other from the remaining region outside of ENSO. Figure 8 compares the results of these decompositions for both the observations and AMIP6 models. Only cloud feedbacks estimated using the cloud kernel technique are shown. At TOA and within ATM, models tend to overestimate the LW feedback in the ENSO and underestimate that in the non-ENSO region compared to observation. It is worth noting that such inverse relationship between ENSO and non-ENSO regions is also present in the SW component. For example, strong negative SW feedback in MRI-ESM2-0 in the ENSO region was accompanied by strong positive SW feedback in the non-ENSO region, and the opposite was true for GISS-E2-1-G. This demonstrates that models are diverse in how their global feedback distributed between ENSO and non-ENSO regions.

To better understand the model behaviors, we show in Figure 9 the cloud responses partitioned by the ISCCP cloud-type classification in the ENSO and non-ENSO regions. When viewing clouds stratified by cloud optical thickness, the observation shows an increase in cloud fraction for optically medium and thick clouds in response to temperature changes in the non-ENSO region, with relatively small changes in the ENSO region. Models can well capture the positive change of medium clouds in the non-ENSO region. However, models tend to underestimate the positive change of thick clouds in the non-ENSO region in comparison with the observation. In addition, models produced larger thin cloud response in both ENSO and non-ENSO regions compared to observations. When viewing clouds stratified by cloud top height, the observations exhibit negative high-topped cloud changes in the ENSO region and positive changes in the non-ENSO region. Most models produced changes almost opposite to the observations, that is, positive high-topped cloud changes in the ENSO region and negative changes

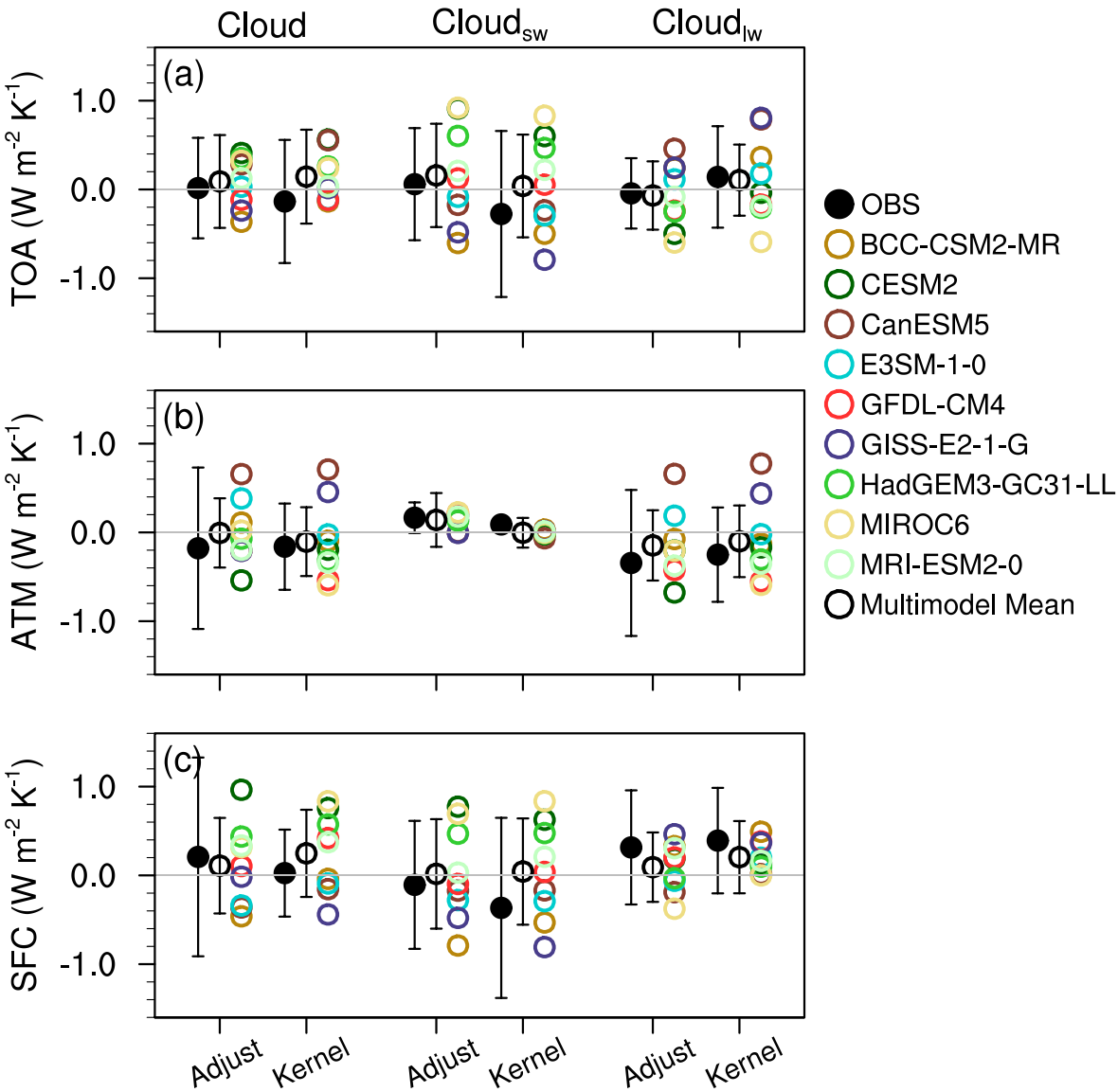

Figure 7. Global average cloud feedback for the observation and AMIP6 models at top of the atmosphere (a), atmospheric column (b), and SFC (c). Two different methods were used for estimating cloud feedback, distinguished by the labels "Adjust" and "Kernel." The error bar in solid circles represents the 95% confidence range in observations, while the error bar in open circles represents the 95% confidence range in models.

in the non-ENSO region. Regarding low-topped clouds, observations show positive changes in both ENSO and non-ENSO regions, whereas models commonly produced negative changes in the ENSO region and positive changes in the non-ENSO region.

Figure 10 shows the corresponding SW and LW cloud feedbacks at TOA decomposed by thin, medium, thick, high, middle, low and clouds, and Figures S4 and S5 in Supporting Information S1 show such decomposition on ATM and SFC. Note that the total cloud feedback shown in Figure 8 is equal to both the sum of the thin, medium, and thick cloud feedbacks and the sum of high, middle, and low cloud feedbacks. Since SW cloud radiative kernel is more sensitive to cloud optical depth (Figure 1a), medium and thick clouds have a greater influence on SW cloud feedback than thin clouds (Figure 10a). Compared to the observation, models tend to overestimate the feedback in the non-ENSO region for medium clouds and underestimate the feedback in the ENSO region for thick clouds. Because the solar zenith angle complicates the computation of SW cloud feedback, there is no clear correspondence between SW cloud feedback and changes of cloud types stratified by optical depth.

Table 2
Global Average SW (LW) Cloud Feedbacks at Top of the Atmosphere, Atmospheric Column, and SFC (W m^{-2} K^{-1})

Cloud feedback (adjusting/kernel)	SW			LW		
	TOA	ATM	SFC	TOA	ATM	SFC
OBS	0.06/−0.28	0.17/0.09	−0.11/−0.37	−0.04/0.14	−0.34/−0.25	0.31/0.39
Multimodel Mean	0.16/0.04	0.14/0.01	0.02/0.04	−0.07/0.10	−0.15/−0.10	0.09/0.21
BCC-CSM2-MR	−0.60/−0.50	0.19/0.03	−0.79/−0.53	0.24/0.36	−0.07/−0.13	0.33/0.49
CESM2	0.91/0.60	0.14/−0.03	0.77/0.63	−0.50/−0.04	−0.68/−0.17	0.19/0.13
CanESM5	−0.17/−0.24	−0.01/−0.07	−0.17/−0.17	0.46/0.79	0.66/0.78	−0.19/0.01
E3SM-1-0	−0.08/−0.29	0.20/−0.01	−0.28/−0.29	0.11/0.18	0.19/−0.02	−0.06/0.20
GFDL-CM4	0.12/0.05	0.22/0.01	−0.10/0.04	−0.24/−0.17	−0.42/−0.55	0.20/0.38
GISS-E2-1-G	−0.48/−0.79	−0.01/0.02	−0.48/−0.81	0.24/0.81	−0.20/0.44	0.46/0.37
HadGEM3-GC31-LL	0.60/0.47	0.13/−0.01	0.47/0.48	−0.25/−0.21	−0.20/−0.30	−0.03/0.10
MIROC6	0.92/0.83	0.23/−0.01	0.69/0.84	−0.60/−0.59	−0.21/−0.59	−0.38/−0.01
MRI-ESM2-0	0.21/0.22	0.18/0.01	0.03/0.21	−0.08/−0.19	−0.37/−0.35	0.31/0.16

With regard to LW cloud feedback, it closely resembles high-topped cloud changes, with relatively small contributions from mid- and low-topped clouds. This is because the LW kernel increases strongly with decreasing P_{top} (Figure 1b), and thus the LW cloud feedback is mostly determined by changes in high-topped clouds. As anticipated, for high-topped clouds, most of the models produced positive feedback in the ENSO region and negative feedback in the non-ENSO regions, contrary to observations. Among all, BCC-CSM2-MR and CanESM5 produced the two largest LW cloud feedbacks in the ENSO region, which is in accordance with the largest high cloud changes shown in Figure 9. Only GFDL-CM4 produced LW cloud feedback that roughly agreed with observations within the uncertainty range. The remaining models failed to reproduce cloud feedback even in sign. For these models, it is the offset between the bias in the ENSO region and the bias in the non-ENSO region that leads to the overall agreement in the global average. Although these compensations would lead to similar global cloud responses, the compensating errors are likely to translate into diversity and uncertainty in long-term cloud feedback.

3.4. Kernel Sensitivity Study

The construction of radiative kernels requires perturbation to basic fields such as temperature and moisture, which can be either from climate models, reanalysis data sets or observations, thus introducing uncertainty in the resulting kernels. In addition, the difference in radiative transfer algorithms may also contribute to the uncertainty. This subsection examines the extent to which the estimated cloud feedback is sensitive to the kernel used. For the adjusting method, we use the alternative kernel of Huang et al. (2017), which was built based on 5-year ERA-Interim reanalysis, compared to the observation-based radiative kernel from 1-year CloudSat/CALIPSO data set (Kramer et al., 2019). For the cloud radiative kernel, the alternative kernel of Zhang et al. (2021) is used, in which the cloud vertical structure was based on a combination of rawinsonde climatology and CloudSat-CALIPSO climatology, while in Zhou et al. (2022) the statistical relationships between P_{top}, P_{bot} and τ were calculated from collocated MODIS-CloudSat climatology.

Table 3
Global Average NET Cloud Feedbacks at Top of the Atmosphere, Atmospheric Column, and SFC (W m^{-2} K^{-1})

Cloud feedback		NET (SW + LW)		
		TOA	ATM	SFC
OBS	Adjust	0.02 ± 0.57	−0.17 ± 0.91	0.19 ± 1.12
	Kernel	−0.14 ± 0.69	−0.16 ± 0.49	0.02 ± 0.49
	Avg	−0.06 ± 0.63	−0.17 ± 0.70	0.11 ± 0.81
Multimodal Mean	Adjust	0.09 ± 0.28	−0.01 ± 0.36	0.10 ± 0.46
	Kernel	0.14 ± 0.28	−0.09 ± 0.44	0.23 ± 0.45
	Avg	0.12 ± 0.28	−0.05 ± 0.40	0.17 ± 0.46

Figure 11 shows a scatterplot of cloud feedbacks calculated using the Kramer et al. (2019) kernel versus those calculated using the Huang et al. (2017) kernel. Each point represents the global average feedback computed at TOA, ATM and SFC for the observation and AMIP6 models. For cloud feedback at TOA, the points collapse reasonably well on the 1:1 line. The SW points fall slightly below the 1:1 line, and the LW points fall slightly above the 1:1 line. The difference between observation and the multimodel mean is reduced from 0.09 to 0.06 W m^{-2} K^{-1} for SW cloud feedback, and almost keep unchanged for LW cloud feedback. Although the dispersion is relatively

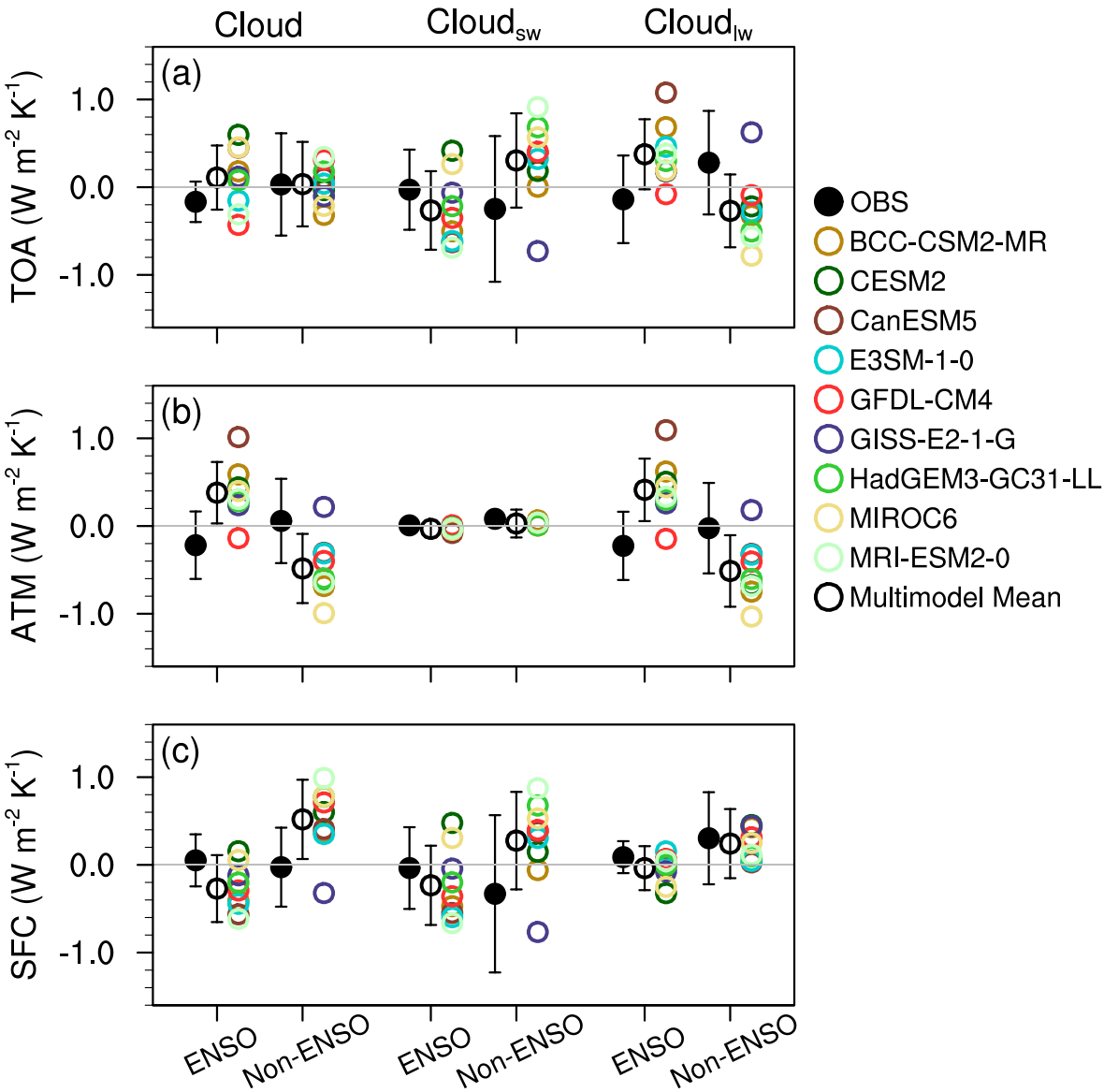

Figure 8. Same as Figure 7, but cloud feedbacks estimated using the cloud kernel technique are decomposed into El Niño–Southern Oscillation (ENSO) and non-ENSO regions.

larger at SFC and ATM, the change of the difference between observation and the multimodel mean is very small, mostly within the range of 0.03 W m^{-2} K^{-1}. Therefore, the results are qualitatively unchanged when replaced with the Huang et al. (2017) kernel.

Figure 12 shows the scatterplot of cloud feedbacks calculated using the cloud radiative kernel of Zhou et al. (2022) versus those calculated using the kernel of Zhang et al. (2021). The points are more dispersed around the 1:1 line than those seen in Figure 11, indicating cloud feedback is more sensitive to the kernel used in the cloud radiative kernel technique than in the adjusting method. Consequently, the change in the difference between the observation and the multimodel mean is relatively larger, up to 0.1 W m^{-2} K^{-1} for LW cloud feedback, and a relatively small value of 0.04 W m^{-2} K^{-1} for SW cloud feedback. Considering that 0.1 W m^{-2} K^{-1} is still a small value, much smaller than the uncertainty range shown in Figure 7, the main conclusions are unaffected when replaced with the Zhang et al. (2021) kernel.

The differences shown in Figure 12 are mainly attributed to the differences in cloud radiative kernels, as shown in Figure 13. Compared to the kernel of Zhou et al. (2022), the kernel of Zhang et al. (2021) produces larger values

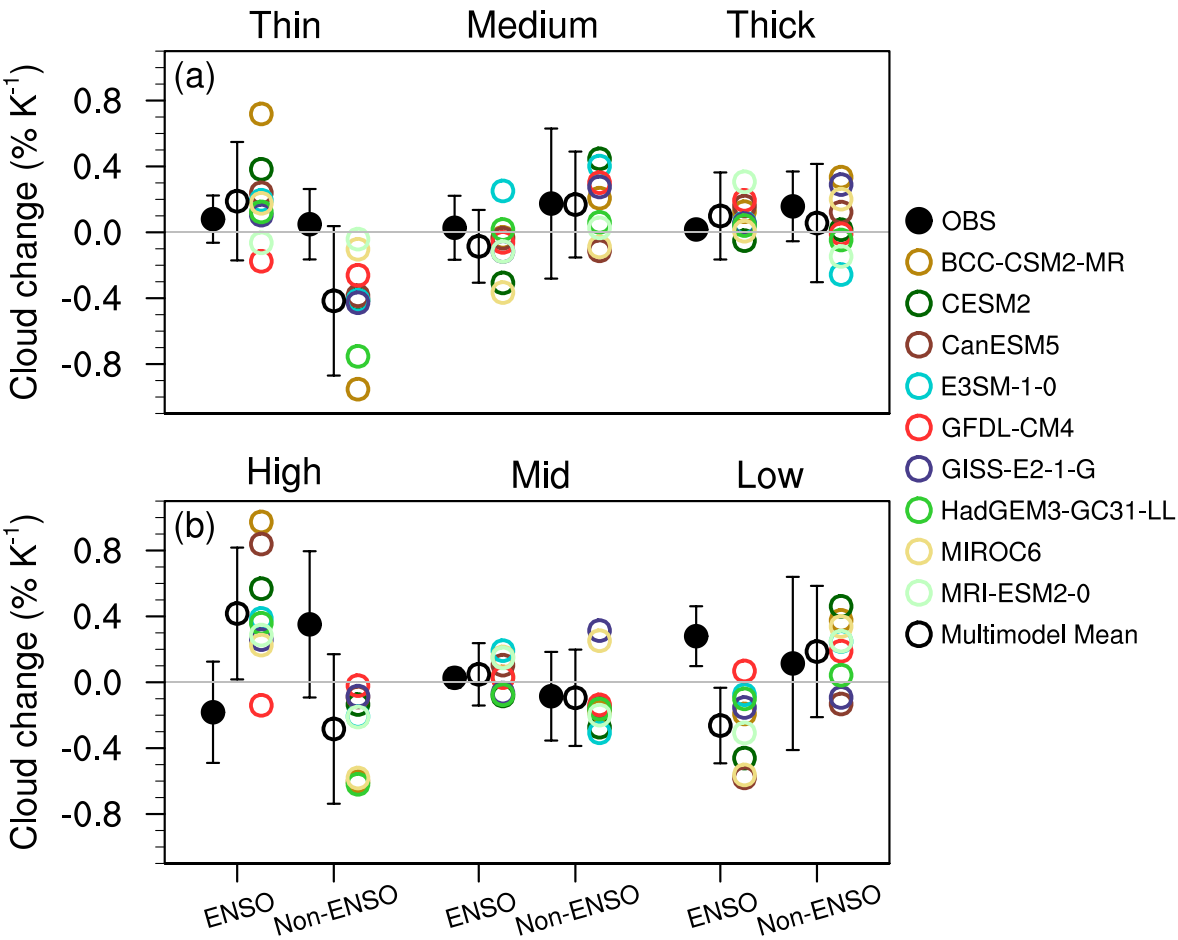

Figure 9. Observed and model-simulated cloud response stratified by cloud optical thickness (a) and cloud top height (b) in El Niño–Southern Oscillation (ENSO) and non-ENSO regions. The error bar in solid circles represents the 95% confidence range in observations, while the error bar in open circles represents the 95% confidence range in models.

of SW and LW overcast CREs per percent cloud fraction change for optically thin clouds, and smaller values for optically medium and thick clouds at TOA. The difference map for the SW kernel at SFC is similar to that at TOA. For LW at SFC, the Zhang et al. (2021) kernel produces larger overcast CREs for low-topped clouds and smaller overcast CREs for high-topped clouds relative to the Zhou et al. (2022) kernel. Within ATM, the Zhang et al. (2021) kernel produces larger LW overcast CREs for almost all cloud types except for low-topped thin clouds, which is why LW ATM cloud feedbacks computed with the Zhang (2021) kernel are always larger than those computed with the Zhou et al. (2022) kernel (Figure 12d).

4. Conclusion

This study investigated the observed cloud feedbacks at TOA, ATM and SFC based on short-term climate variations during 2000–2014, which were then used to validate short-term cloud feedbacks estimated from 9 AMIP6 models. Two different methods were used to estimate the cloud feedback: the method of adjusting changes in cloud radiative effects (Shell et al., 2008; Soden et al., 2008), and the cloud radiative kernel technique (Zelinka et al., 2012).

For the adjusting method, we use the observation-based radiative kernels from CloudSat/CALIPSO (Kramer et al., 2019) to break down the feedbacks into individual components. For the cloud radiative kernel, we use the TOA and SFC cloud radiative kernels developed by Zhou et al. (2022). The cloud feedbacks calculated by the two techniques are generally in good agreement for both observations and AMIP6 models. Both methods show that the observed ATM net cloud feedback is about -0.17 W m^{-2} K^{-1}, suggesting cloud changes act to increase the radiative cooling of the atmosphere during the period 2000–2014. By averaging the two estimations, the global

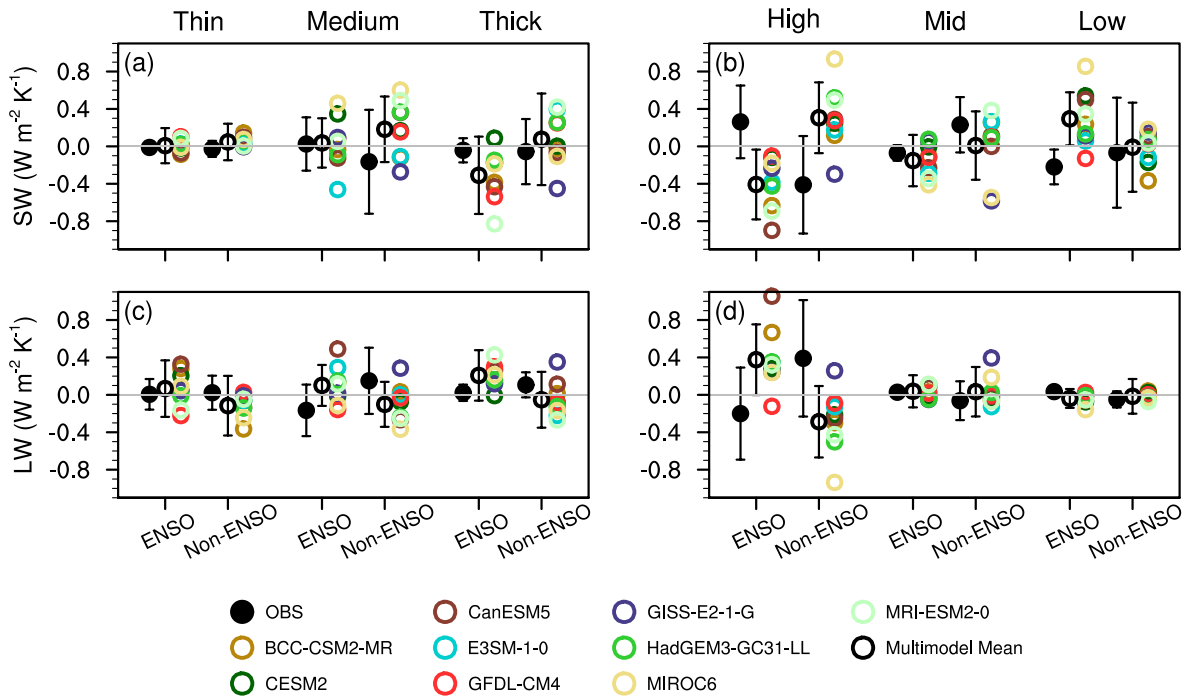

Figure 10. Observed and model-produced SW (a, b) and LW (c, d) top of the atmosphere cloud feedback stratified by cloud optical thickness (a, c) and cloud top height (b, d) in El Niño–Southern Oscillation (ENSO) and non-ENSO regions. The error bar in solid circles represents the 95% confidence range in observations, while the error bar in open circles represents the 95% confidence range in models.

mean net cloud feedback is -0.06 ± 0.63 W m^{-2} K^{-1} at TOA, -0.17 ± 0.70 W m^{-2} K^{-1} within ATM, and 0.11 ± 0.81 W m^{-2} K^{-1} at SFC.

Although most models produced global average feedbacks that agreed, within uncertainty ranges, with the observations, there were a few models that produced values outside the observed uncertainty range, especially for the feedbacks at SFC and ATM. This demonstrates that models have a large diversity in how the TOA feedbacks are distributed between SFC and ATM. Sensitivity tests show that the main conclusions still hold when alternative kernels are used.

By decomposing the global average feedback into two parts—one from the ENSO region and the other from the remaining region outside of the ENSO—results showed that cloud feedback in these two regions is often inversely related. The cloud radiative kernel technique allows one to attribute cloud feedback to specific cloud types. The observations exhibited negative high-topped cloud changes in the ENSO region, which were largely offset by positive changes in the non-ENSO region. Most models produced changes that were almost opposite to the observed values. Correspondingly, this leads to an overestimation of LW cloud feedback in the ENSO region and an underestimation of LW cloud feedback in the non-ENSO region in the models. It was the offset between the bias in the two regions that led to the agreement of the global average with observations. However, these compensating errors are likely to translate into diversity and uncertainty in long-term cloud feedback. Therefore, it calls for models to simulate accurate cloud responses in both the ENSO and non-ENSO regions to further improve the model fidelity.

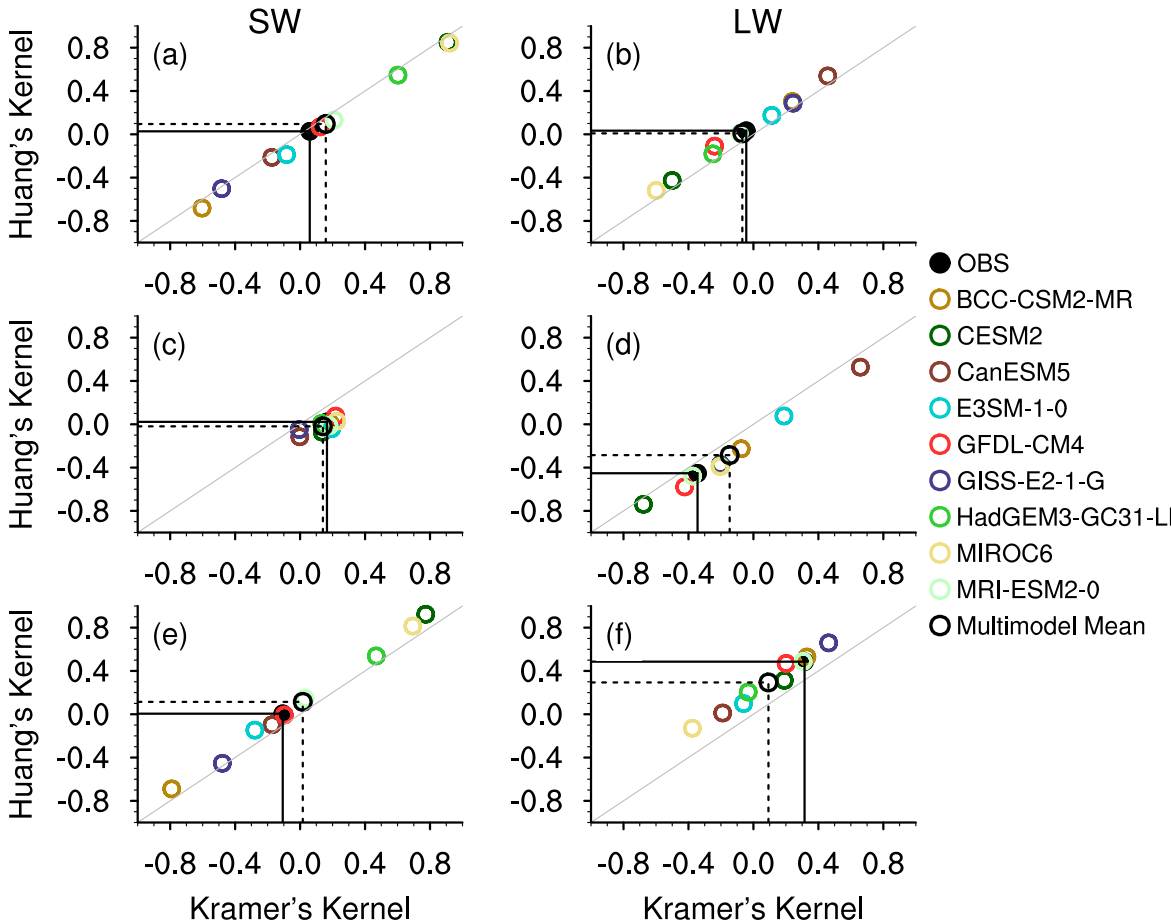

Figure 11. Scatterplot of cloud feedback at top of the atmosphere (a, b), atmospheric column (c, d), and SFC (e, f) estimated using Kramer's Kernel versus using Huang's Kernel under the adjusting method. The left and right columns are the SW and LW components. Unit: W m^{-2} K^{-1}.

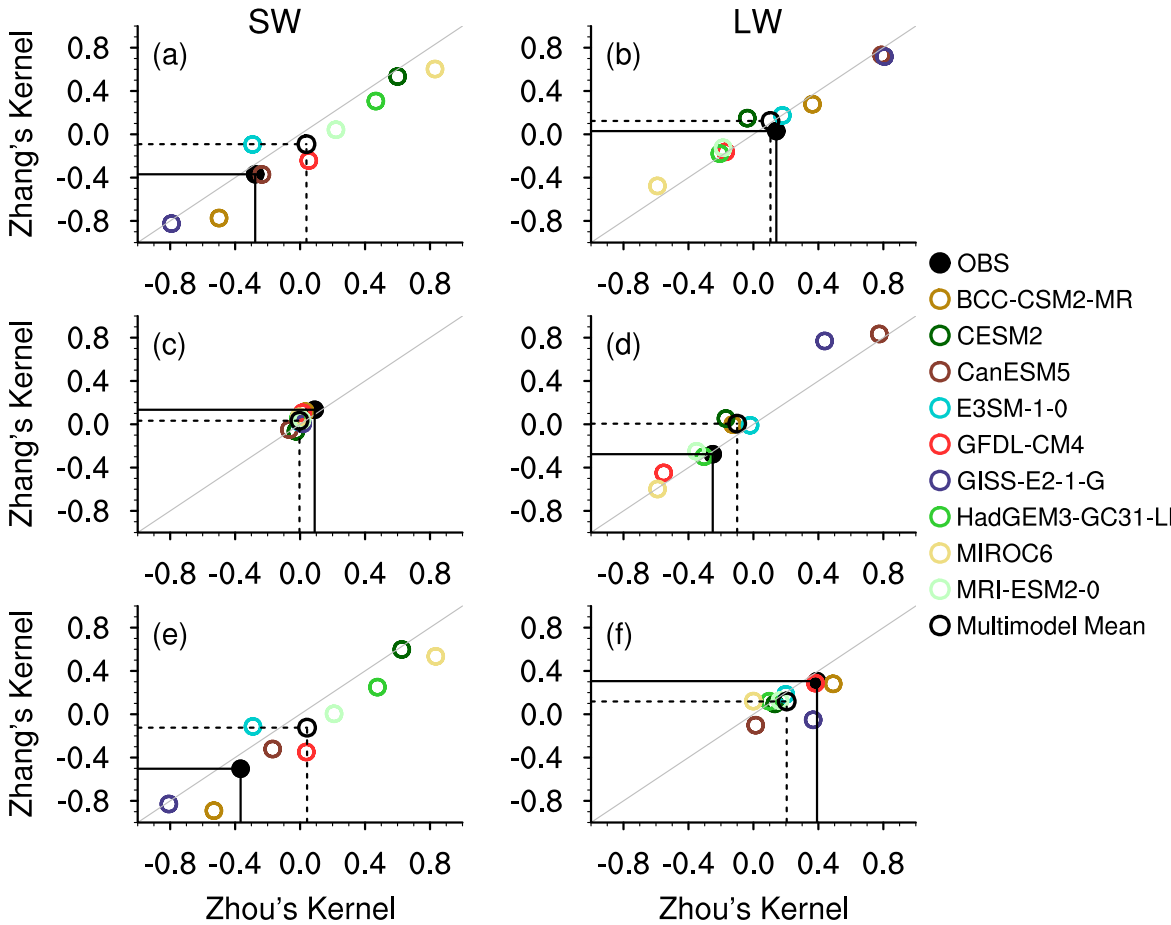

Figure 12. Scatterplot of cloud feedback at top of the atmosphere (a, b), atmospheric column (c, d), and SFC (e, f) estimated using Zhou's Kernel versus using Zhang's Kernel under the cloud kernel technique. The left and right columns are the SW and LW components. Unit: W m^{-2} K^{-1}.

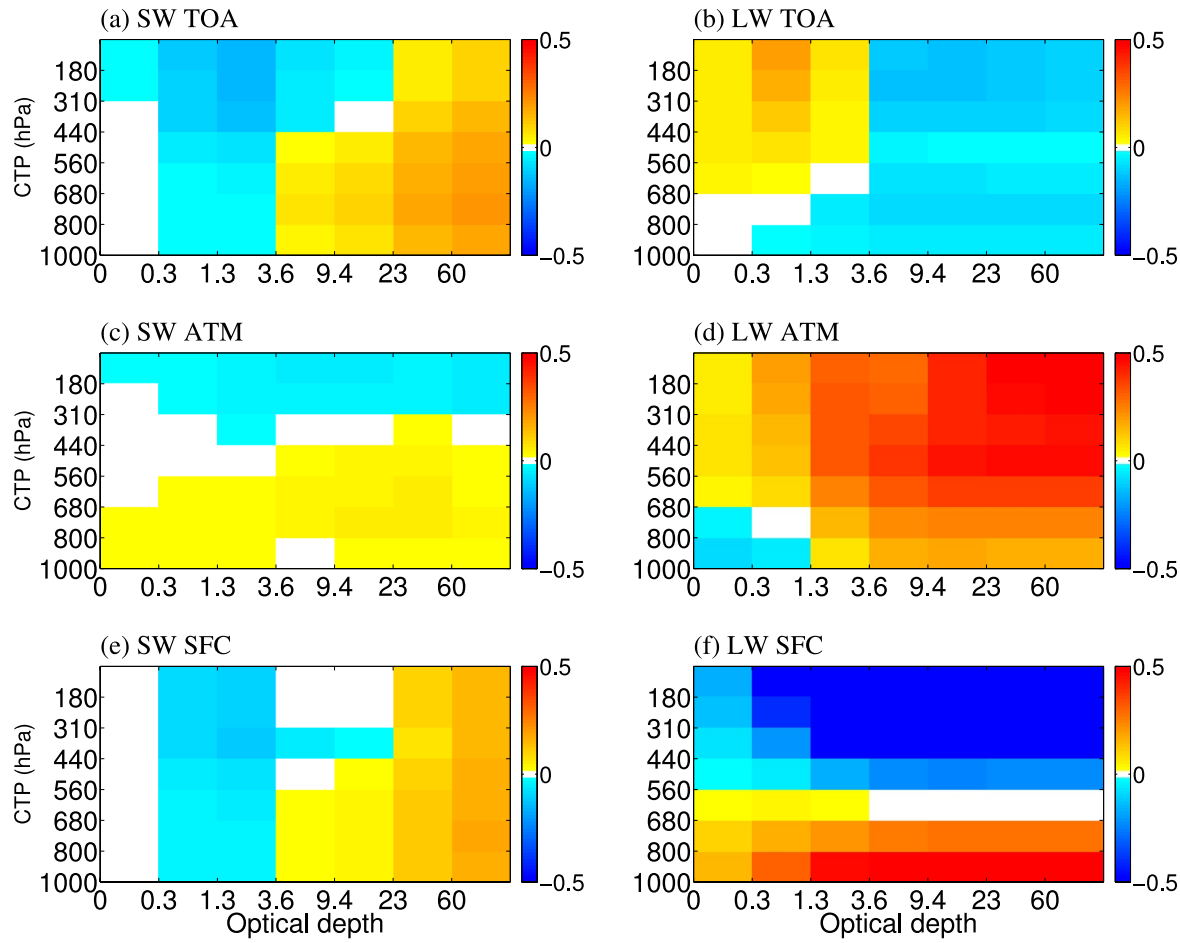

Figure 13. Difference of global and annual mean SW (a, c, e) and LW (b, d, f) cloud radiative kernels at top of the atmosphere (a, b), atmospheric column (c, d), and SFC (e, f) between Zhang's kernel and Zhou's kernel. (Unit: W $m^{-2}\%^{-1}$).

Data Availability Statement

All data used in this study are available to the public. The ERA-interim reanalysis data can be download from the website at https://www.ecmwf.int/en/forecasts/datasets/reanalysis-datasets/era-interim. Cloud and the Earth's Radiant Energy System Energy Balanced and Filled (EBAF) TOA Monthly means are available at https://asdc.larc.nasa.gov/data/CERES/EBAF/TOA_Edition4.1/. (NASA/LARC/SD/ASDC, 2019). MODIS (MOD08_M3) data is available at https://modis.gsfc.nasa.gov/. The ISCCP (HGG) data is accessible from https://isccp.giss.nasa.gov/. The AMIP6 data used in this study are available from https://esgf-node.llnl.gov/search/cmip6/. The radiative kernel form Kramer can be found at https://climate.earth.miami.edu/data/radiative-kernels/.

Acknowledgments
The authors thank the three anonymous reviewers for their constructive comments that helped to clarify and improve the original paper. Thanks also go to Drs. Kramer R, Zhou C. (2021), Huang Y. (2022), and Zhang Y. (2021) for making their radiative kernels available to the public. This work was jointly supported by the National Natural Science Foundation of China (Grants 42175165, 42205041), the National Key Scientific and Technological Infrastructure project "Earth System Science Numerical Simulator Facility" (EarthLab), and State Key Laboratory of Tropical Oceanography, South China Sea Institute of Oceanology, Chinese Academy of Sciences (Project No. LTO2212).

References

Allen, M. R., & Ingram, W. J. (2002). Constraints on future changes in climate and the hydrologic cycle. *Nature*, *419*(6903), 224–232. https://doi.org/10.1038/nature01092

Andrews, T., Forster, P. M., & Groegory, J. M. (2009). A surface energy perspective on climate change. *Journal of Climate*, *22*(10), 2557–2570. https://doi.org/10.1175/2008JCLI2759.1

Bony, S., & Dufresne, J. L. (2005). Marine boundary layer clouds at the heart of tropical cloud feedback uncertainties in climate models. *Geophysical Research Letters*, *32*(20), L20806. https://doi.org/10.1029/2005GL023851

Ceppi, P., Brient, F., Zelinka, M., & Hartmann, D. (2017). Cloud feedback mechanisms and their representation in global climate models. *WIREs Clim Change, Advanced Review*, *8*(4), e465. https://doi.org/10.1002/wcc.46

Cesana, G., Suselj, K., & Brient, F. (2017). On the dependence of cloud feedbacks on physical parameterizations in WRF aquaplanet simulations. *Geophysical Research Letters*, *44*(20), 10762–10771. https://doi.org/10.1002/2017GL074820

Chao, L. W., Muller, J. C., & Dessler, A. E. (2022). Impacts of the unforced pattern effect on the cloud feedback in CERES observations and climate models. *Geophysical Research Letters*, *49*(2), e2021GL096299. https://doi.org/10.1029/2021GL096299

Colman, R. A. (2003). A comparison of climate feedbacks in general circulation models. *Climate Dynamics*, *20*(7), 865–873. https://doi.org/10.1007/s00382-003-0310-z

Colman, R. A., & Power, S. B. (2010). Atmospheric radiative feedbacks associated with transient climate change and climate variability. *Climate Dynamics*, *34*(7), 919–933. https://doi.org/10.1007/s00382-009-0541-8

Dee, D. P., Uppala, S. M., Simmons, A. J., Berrisford, P., Poli, P., Kobayashi, S., et al. (2011). The ERA-Interim reanalysis: Configuration and performance of the data assimilation system. *Quarterly Journal of the Royal Meteorological Society*, *137*(656), 553–597. https://doi.org/10.1002/qj.828

Dessler, A. E. (2010). A determination of the cloud feedback from climate variations over the past decade. *Science*, *330*(6010), 1523–1527. https://doi.org/10.1126/science.1192546

Dessler, A. E. (2013). Observations of climate feedbacks over 2000–10 and comparisons to climate models. *Journal of Climate*, *26*(1), 333–342. https://doi.org/10.1175/JCLI-D-11-00640.1

Eyring, V., Bony, S., Meehl, G. A., Senior, C. A., Stevens, B., Stouffer, R. J., & Taylor, K. E. (2016). Overview of the Coupled Model Intercomparison Project Phase 6 (CMIP6) experimental design and organization. *Geoscientific Model Development*, *9*(5), 1937–1958. https://doi.org/10.5194/gmd-9-1937-2016

Gregory, J. M., Ingram, W. J., Palmer, M. A., Jones, G. S., Stott, P. A., Thorpe, R. B., et al. (2004). A new method for diagnosing radiative forcing and climate sensitivity. *Geophysical Research Letters*, *31*(3), L03205. https://doi.org/10.1029/2003GL018747

Huang, Y. (2022). ERA-interim reanalysis based radiative kernels (Version 1) [Dataset]. https://doi.org/10.17632/3drx8fmmz9.1

Huang, Y., Xia, Y., & Tan, X. (2017). On the pattern of CO_2 radiative forcing and poleward energy transport. *Journal of Geophysical Research: Atmospheres*, *122*(20), 10578–10593. https://doi.org/10.1002/2017JD027221

Kramer, R. J., Matus, A. V., Soden, B. J., & L'Ecuyer, T. S. (2019). Observation-based radiative kernels from CloudSat/CALIPSO. *Journal of Geophysical Research: Atmospheres*, *124*(10), 5431–5444. https://doi.org/10.1029/2018JD029021

Lambert, F. H., Webb, M. J., Yoshimori, M., & Yokohata, T. (2015). The cloud radiative effect on the atmospheric energy budget and global mean precipitation. *Climate Dynamics*, *44*(7–8), 2301–2325. https://doi.org/10.1007/s00382-014-2174-9

Liu, M., Zhang, H., Wang, F., Wang, Z., Wang, F., Wang, H., & Chen, B. (2022). Quantifying long-term cloud feedback over East Asia combining with radiative kernels and CMIP6 data. *Climate Dynamics*, *61*(4), 341–356. https://doi.org/10.1007/s00382-022-06577-7

Loeb, N. G., Wang, H., Allan, R., Andrews, T., Armour, K., Cole, J. N. S., et al. (2020). New generation of climate models track recent unprecedented changes in Earth's radiation budget observed by CERES. *Geophysical Research Letters*, *47*(5), e2019GL086705. https://doi.org/10.1029/2019GL086705

Lu, J., & Cai, M. (2009). Seasonality of polar surface warming amplification in climate simulations. *Geophysical Research Letters*, *36*(16), L16704. https://doi.org/10.1029/2009GL040133

Marchand, R. (2013). Trends in ISCCP, MISR, and MODIS cloud-top-height and optical-depth histograms. *Journal of Geophysical Research: Atmospheres*, *118*(4), 1941–1949. https://doi.org/10.1002/jgrd.50207

Miao, H., Wang, X., Liu, Y., & Wu, G. (2021). A regime-based investigation into the errors of CMIP6 simulated cloud radiative effects using satellite observations. *Geophysical Research Letters*, *48*(18), e2021GL095399. https://doi.org/10.1029/2021GL095399

Mitchell, J., Wilson, C., & Cunnington, W. (1987). On CO_2 climate sensitivity and model dependence of results. *Quarterly Journal of the Royal Meteorological Society*, *113*(475), 293–322. https://doi.org/10.1002/qj.49711347517

NASA/LARC/SD/ASDC. (2019). CERES energy balanced and filled (EBAF) TOA and surface monthly means data in netCDF Edition 4.1 [Dataset]. NASA Langley Atmospheric Science Data Center DAAC. https://doi.org/10.5067/TERRA-AQUA/CERES/EBAF_L3B.004.1

Platnick, S., King, M., & Hubanks, P. (2015). *MODIS atmosphere L3 monthly product. NASA MODIS adaptive processing system*. Goddard Space Flight Center. https://doi.org/10.5067/MODIS/MOD08_M3.061

Previdi, M. (2010). Radiative feedbacks on global precipitation. *Environmental Research Letters*, *5*(2), 025211. https://doi.org/10.1088/1748-9326/5/2/025211

Previdi, M., & Liepert, B. (2012). The vertical distribution of climate forcings and feedbacks from the surface to top of atmosphere. *Climate Dynamics*, *39*(3–4), 941–951. https://doi.org/10.1007/s00382-011-1233-8

Raghuraman, S. P., Paynter, D., Menzel, R., & Ramaswamy, V. (2023). Forcing, cloud feedbacks, cloud masking, and internal variability in the cloud radiative effect satellite record. *Journal of Climate*, *36*(12), 4151–4167. https://doi.org/10.1175/JCLI-D-22-0555.1

Raghuraman, S. P., Paynter, D., & Ramaswamy, V. (2019). Quantifying the drivers of the clear sky greenhouse effect, 2000–2016. *Journal of Geophysical Research: Atmospheres*, *124*(21), 11354–11371. https://doi.org/10.1029/2019JD031017

Shell, K. M., Kiehl, J. T., & Shields, C. A. (2008). Using the radiative kernel technique to calculate climate feedbacks in NCAR's Community Atmospheric Model. *Journal of Climate*, *21*(10), 2269–2282. https://doi.org/10.1175/2007JCLI2044.1

Sherwood, S. C., Webb, M. J., Annan, J. D., Armour, K. C., Forster, P. M., Hargreaves, J. C., et al. (2020). An assessment of Earth's climate sensitivity using multiple lines of evidence. *Reviews of Geophysics*, *58*(4), e2019RG000678. https://doi.org/10.1029/2019RG000678

Soden, B., Held, I., Colman, R. A., Shell, K., Kiehl, J. T., & Shields, C. A. (2008). Quantifying climate feedbacks using radiative kernels. *Journal of Climate*, *21*(14), 3504–3520. https://doi.org/10.1175/2007JCLI2110.1

Stephens, G., & Ellis, T. (2008). Controls of global-mean precipitation increases in global warming GCM experiments. *Journal of Climate*, *21*(23), 6141–6155. https://doi.org/10.1175/2008JCLI2144.1

Stephens, G. L. (2005). Cloud feedbacks in the climate system: A critical review. *Journal of Climate*, *18*(2), 237–273. https://doi.org/10.1175/JCLI-3243.1

Wang, F., Zhang, H., Qi, C., Min, Z., & You, T. (2020). Analysis of short-term cloud feedback in East Asia using cloud radiative kernels. *Advances in Atmospheric Sciences*, *37*(9), 1007–1018. https://doi.org/10.1007/s00376-020-9281-9

Wang, F., Zhang, H., Wang, Q., Xie, B., Zhou, X., & Liu, Q. (2023). An assessment of short-term global and East Asian local climate feedbacks using new radiative kernels. *Climate Dynamics*, *60*(5–6), 1329–1349. https://doi.org/10.1007/s00382-022-06369-z

Wang, X., Miao, H., Liu, Y., Bao, Q., He, B., Li, J., & Zhao, Y. (2022). The use of satellite data-based "critical relative humidity" in cloud parameterization and its role in modulating cloud feedback. *Journal of Advances in Modeling Earth Systems*, *14*(10), e2022MS003213. https://doi.org/10.1029/2022MS003213

Yan, X., Boyer, T., Trenberth, K., Karl, T., Xie, S., Nieves, V., et al. (2016). The global warming hiatus: Slowdown or redistribution? *Earth's Future*, *4*(11), 472–482. https://doi.org/10.1002/2016EF000417

Young, A., Knapp, K., Inamdar, A., Hankins, W., & Rossow, W. (2018). The International satellite cloud climatology project H-series climate data record product. *Earth System Science Data*, *10*(1), 583–593. https://doi.org/10.5194/essd-10-583-2018

Zelinka, M. D., Klein, S. A., Qin, Y., & Myers, T. A. (2022). Evaluating climate models' cloud feedbacks against expert judgment. *Journal of Geophysical Research: Atmospheres*, *127*(2), e2021JD035198. https://doi.org/10.1029/2021JD035198

Zelinka, M. D., Myers, T. A., McCoy, D. T., Po-Chedley, S., Caldwell, P. M., Ceppi, P., et al. (2020). Causes of higher climate sensitivity in CMIP6 models. *Geophysical Research Letters*, *47*(1), e2019GL085782. https://doi.org/10.1029/2019GL085782

Zelinka, M. D., Stephens, A. K., & Hartmann, D. (2012). Computing and partitioning cloud feedbacks using cloud property histograms. Part I: Cloud radiative kernels. *Journal of Climate*, *25*(11), 3715–3735. https://doi.org/10.1175/JCLI-D-11-00248.1

Zhang, M. H., Hack, J. J., Kiehl, J. T., & Cess, R. D. (1994). Diagnostic study of climate feedback processes in atmospheric general circulation models. *Journal of Geophysical Research*, *99*(D3), 5525–5537. https://doi.org/10.1029/93JD03523

Zhang, R. D., Wang, H. L., Fu, Q., Pendergrass, A. G., Wang, M. H., Yang, Y., et al. (2018). Local radiative feedbacks over the Arctic based on observed short-term climate variations. *Geophysical Research Letters*, *45*(11), 5761–5770. https://doi.org/10.1029/2018GL077852

Zhang, R. D., Wang, H. L., Fu, Q., & Rasch, P. J. (2020). Assessing global and local radiative feedbacks based on AGCM simulations for 1980–2014/2017. *Geophysical Research Letters*, *47*(12), e2020GL088063. https://doi.org/10.1029/2020GL088063

Zhang, Y. (2021). ISCCP-FH Cloud radiative kernel for TOA and surface from the ISCCP-FH flux production code based on ISCCP-H data [Dataset]. https://doi.org/10.5281/zenodo.4677580

Zhang, Y., Jin, Z., & Sikand, M. (2021). The top-of-atmosphere, surface and atmospheric cloud radiative kernels based on ISCCP-H datasets: Method and evaluation. *Journal of Geophysical Research: Atmospheres*, *126*(24), e2021JD035053. https://doi.org/10.1029/2021JD035053

Zhao, Y., Li, J., Zhang, W., Deng, C., & Li, Y. (2022). Cloud response is significantly biased by CMIP6 over the Tibetan Plateau. *Geophysical Research Letters*, *49*(17), e2022GL100903. https://doi.org/10.1029/2022GL100903

Zhou, C. (2021). TOA and surface cloud radiative kernels calculated with RRTM (Version v3) [Dataset]. Zenodo. https://doi.org/10.5281/zenodo.5176193

Zhou, C., Liu, Y. C., & Wang, Q. (2022). Calculating the climatology and anomalies of surface cloud radiative effect using cloud property histograms and cloud radiative kernels. *Advances in Atmospheric Sciences*, *39*(2), 2124–2136. https://doi.org/10.1007/s00376-021-1166-z

Zhou, C., Zelinka, M. D., Dessler, A. E., & Klein, S. A. (2015). The relationship between inter-annual and long-term cloud feedbacks. *Geophysical Research Letters*, *42*(23), 10463–10469. https://doi.org/10.1002/2015GL066698

Zhou, C., Zelinka, M. D., Dessler, A. E., & Yang, P. (2013). An analysis of the short-term cloud feedback using MODIS data. *Journal of Climate*, *26*(13), 4803–4815. https://doi.org/10.1175/JCLI-D-12-00547.1

Zhou, C., Zelinka, M. D., & Klein, S. A. (2016). Impact of decadal cloud variations on the Earth's energy budget. *Nature Geoscience*, *9*(12), 871–874. https://doi.org/10.1038/ngeo2828

Zhu, P., Hack, J. J., Kiehl, J. T., & Bretherton, C. S. (2007). Climate sensitivity of tropical and subtropical marine low cloud amount to ENSO and global warming due to doubled CO2. *Journal of Geophysical Research*, *112*(D17), D17108. https://doi.org/10.1029/2006JD008174